



## Research Paper

Cerium modified birnessite-type MnO<sub>2</sub> for gaseous formaldehyde oxidation at low temperatureLin Zhu<sup>a</sup>, Jinlong Wang<sup>a</sup>, Shaopeng Rong<sup>a</sup>, Haiyan Wang<sup>b,\*,\*\*</sup>, Pengyi Zhang<sup>a,c,\*</sup><sup>a</sup> State Key Joint Laboratory of Environment Simulation and Pollution Control, School of Environment, Tsinghua University, Beijing 100084, China<sup>b</sup> State Key Laboratory of Environmental Criteria and Risk Assessment, Chinese Research Academy of Environmental Sciences, Beijing 100012, China<sup>c</sup> Beijing Key Laboratory for Indoor Air Quality Evaluation and Control, Beijing 100084, China

## ARTICLE INFO

## Article history:

Received 7 September 2016

Received in revised form 14 March 2017

Accepted 7 April 2017

Available online 8 April 2017

## Keywords:

Cerium modified birnessite-type MnO<sub>2</sub>

Grain boundary

Oxygen vacancy

HCHO oxidation

## ABSTRACT

Cerium modified birnessite-type manganese dioxides (Ce-MnO<sub>2</sub>) with different doping ratios were prepared by a redox reaction of KMnO<sub>4</sub> with (NH<sub>4</sub>)<sub>2</sub>C<sub>2</sub>O<sub>4</sub> in the presence of Ce(NO<sub>3</sub>)<sub>3</sub>. The as-synthesized Ce-MnO<sub>2</sub> samples were characterized by XRD, SEM, TEM, BET, XPS, ICP-AES, H<sub>2</sub>-TPR, Raman and *in situ* DRIFTS. The results indicate that doping of cerium significantly enhance the performance of birnessite for HCHO removal at low temperature. Ce-MnO<sub>2</sub>(1:10) with the nominal Ce/Mn ratio of 1:10 exhibited the best activity and achieved complete HCHO conversion at 100 °C and better activity at room temperature than undoped birnessite. Upon the doping of cerium, the growth of MnO<sub>2</sub> crystal was inhibited, leading to smaller particle size and higher specific surface. In addition, CeO<sub>2</sub> nanocrystal formed even at low doping ratio (0.1:10), resulting in close contact between CeO<sub>2</sub> and MnO<sub>2</sub> nanocrystals. As a result, the doped material owned higher content of oxygen vacancies and surface adsorbed oxygen species, which contributed to its high activity for HCHO oxidation. This investigation provides a new point of view about how to design an inexpensive efficient catalyst for indoor air purification via introducing appropriate content of cerium.

© 2017 Published by Elsevier B.V.

## 1. Introduction

Formaldehyde (HCHO) is known as one of the major indoor air pollutants, which is mainly released from wooden furniture and construction materials [1,2]. Human health may be damaged during long-term exposure to formaldehyde. Catalytic oxidation of HCHO into CO<sub>2</sub> over metal oxide catalyst is a promising way to remove indoor HCHO at low temperature. As reported in literatures [3–9], noble-metal-based catalysts can convert HCHO into CO<sub>2</sub> and H<sub>2</sub>O at ambient temperature. However, the application of noble-metal-based catalysts are restricted by their high cost. It's essential to develop a kind of inexpensive high performance catalysts, thus researchers focus more of interest on transition metal oxide catalyst [10,11]. Sekine et al. [12] first found the activity of commercial

MnO<sub>2</sub> for HCHO conversion at room temperature. Since then, researchers have investigated various manganese oxides about their HCHO oxidation activity and mechanism [13–17]. Zhang et al. [18] compared the activity of several MnO<sub>2</sub> with different crystal structures. Chen et al. [19] investigated the tunnel structure effect of MnO<sub>2</sub> on oxidation of HCHO. Wang et al. [20,21] found that water and interlayer cations in birnessite-type MnO<sub>2</sub> played an important role in oxidizing HCHO at room temperature.

Nevertheless, there is a tough challenge to increase the activity at ambient temperature and lower the complete conversion temperature. And researchers have tried to promote the activity of catalysts by element incorporation. Lou et al. [22] suggested a valid strategy, i.e. the dopant is required to possess larger radius, weaker M–O bonding and lower electronegativity to decrease the formation energy of oxygen vacancy. Taking these considerations into account, cerium is a promising candidate to meet demands. MnO<sub>x</sub>–CeO<sub>2</sub> composite catalysts were found to be more attractive than manganese oxides catalysts due to its higher HCHO oxidation activity. Tang et al. [23–25] compared the effects of preparation routes and treated temperature to get the high performance MnO<sub>x</sub>–CeO<sub>2</sub> composite catalyst, and further introduced noble metal to enhance the activity. Quiroz et al. [26] investigated the effect of acid treatment towards MnO<sub>x</sub>–CeO<sub>2</sub> composite catalyst. Liu et al.

\* Corresponding author at: State Key Joint Laboratory of Environment Simulation and Pollution Control, School of Environment, Tsinghua University, Beijing 100084, China.

\*\* Corresponding author at: State Key Laboratory of Environmental Criteria and Risk Assessment, Chinese Research Academy of Environmental Sciences, Beijing 100012, China.

E-mail addresses: [wanghaiyan@craes.org.cn](mailto:wanghaiyan@craes.org.cn) (H. Wang), [zpy@tsinghua.edu.cn](mailto:zpy@tsinghua.edu.cn) (P. Zhang).

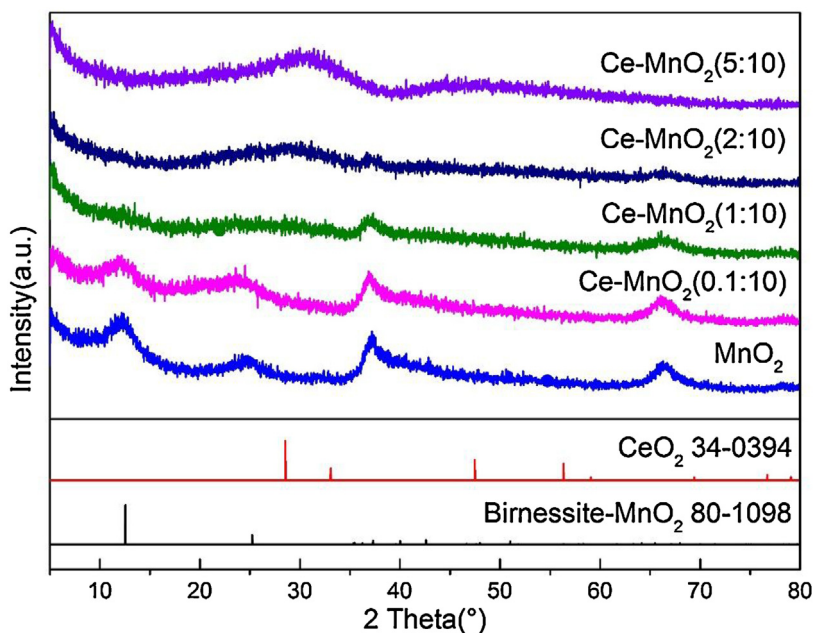


**Fig. 1.** XRD patterns of as-prepared  $\text{MnO}_2$  and cerium-modified  $\text{MnO}_2$  samples.

[27] considered about formaldehyde oxidation over  $\text{MnO}_x\text{-CeO}_2$  composite catalyst. All of the doped catalysts mentioned above shows higher activity than undoped one. Birnessite-type  $\text{MnO}_2$  is a layered manganese oxide which exhibits the best HCHO oxidation activity among manganese oxides with different crystal structures [18,28]. As far as we know, the present investigation first reports the effects of cerium modification on the activity of birnessite for HCHO removal, and reveals that the existence of cerium species and grain boundaries on the surface contribute to enhance the activity of birnessite.

## 2. Experimental

### 2.1. Catalyst preparation

All chemicals used were of analytical grade without further purification. Cerium-birnessite ( $\text{Ce}\text{-MnO}_2$ ) samples were prepared via a redox reaction between  $\text{KMnO}_4$  and  $(\text{NH}_4)_2\text{C}_2\text{O}_4$  with an addition of  $\text{Ce}(\text{NO}_3)_3$ . In a typical preparation process, 1.0 g  $\text{KMnO}_4$ , 0.4 g  $(\text{NH}_4)_2\text{C}_2\text{O}_4\text{:H}_2\text{O}$  and  $\text{Ce}(\text{NO}_3)_3\text{:6H}_2\text{O}$  was dissolved in 130 mL deionized water in an Erlenmeyer flask, which was then shaken in a water bath ( $90^\circ\text{C}$ ) at a frequency of 150 rpm for 10 h. The precipitate was centrifuged and washed many times with deionized water and followed by being dried at  $105^\circ\text{C}$  for 12 h. The addition of  $\text{Ce}(\text{NO}_3)_3\text{:6H}_2\text{O}$  varied with the mole ratio of cerium to manganese ( $\text{Ce}/\text{Mn}$ ), i.e., 0.1:10, 1:10, 2:10 or 5:10. The samples with different doping ratio are referred as  $\text{Ce}\text{-MnO}_2(0.1:10)$ ,  $\text{Ce}\text{-MnO}_2(1:10)$ ,  $\text{Ce}\text{-MnO}_2(2:10)$  and  $\text{Ce}\text{-MnO}_2(5:10)$ , respectively.

### 2.2. Catalyst characterization

XRD analysis was carried out on an X-ray diffractometer (D8-Advance, Bruker, Germany) with  $\text{Cu K}_\alpha$  radiation at 40 kV and 40 mA. Field emission scanning electron microscope (Merlin, Carl Zeiss, Germany) operated at 5 kV was used to obtain FESEM images. The samples were sputter-coated with carbon. Transmission electron microscope (JEOL 2011, JEOL, Japan) with an accelerating voltage of 150 kV was applied to TEM observations. EDS elemental mapping was also collected on a transmission electron microscope

(JEM 2010, JEOL, Japan) with an accelerating voltage of 120 kV. All samples were dispersed in ethanol and deposited on copper grids.

Nitrogen adsorption-desorption (Autosorb-1MP, Quantachrome, USA) experiments were performed to confirm about the BET specific surface area, which was calculated by the multipoint method. The degassed temperature was set as  $200^\circ\text{C}$  for 4 h before the measurement. XPS analysis was carried out on an X-ray photoelectron spectrometer (ESCALAB 250Xi, Thermo Fisher, USA) with a pass energy of 30 eV and  $\text{Al K}_\alpha$  as an X-ray excitation source to investigate the chemical states of surface elements. The binding energy was calibrated with the C 1s line (284.8 eV). Elemental analysis was conducted on an ICP-AES spectrometer (Vista-MPX, VARIAN, USA).

$\text{H}_2\text{-TPR}$  was carried out on an adsorption apparatus (AutoChem 2920, Micromeritics, USA). The as-synthesized samples (50 mg) were loaded into a quartz reactor and pretreated with He (50 mL/min) at  $105^\circ\text{C}$  for 1 h. The reactor cooled down to ambient temperature and then rose at a ramp of  $5^\circ\text{C}/\text{min}$  to  $500^\circ\text{C}$  with the reducing gas (5%  $\text{H}_2/\text{Ar}$ ) at a flow rate of 60 mL/min. Raman spectroscopy was recorded on a confocal Raman microscope (inVia, Renishaw, Britain) with 0.1% laser intensity and an accumulation of 500 scans, using  $\text{Ar}^+$  laser (514.5 nm) as the excitation source. *In situ* DRIFTS was performed on a FTIR spectrometer (NICOLET 6700, Micromeritics, USA) with an *in situ* cell to clarify the intermediate species during HCHO oxidation. All spectra were recorded with a resolution of  $4\text{ cm}^{-1}$  and an accumulation of 32 scans. HCHO ( $\sim 80$  ppm) was injected into the cell at a flow rate of 30 mL/min with the synthetic air as the balance gas.

### 2.3. Evaluation of HCHO removal activity

Dynamic test over as-synthesized samples was performed to evaluate the HCHO removal activity. 100 mg samples (40–60 meshes) was loaded into a quartz reactor with inner diameter of 6 mm. The concentration of HCHO and relative humidity (RH) was determined by adjusting the ratio among gaseous HCHO, dry air and humid air. The feed gas using paraformaldehyde as the gaseous HCHO source was set at  $\sim 190$  ppm. As for HCHO generation, the volatile speed of gaseous HCHO was stable, which was determined by the certain temperature of water bath ( $35^\circ\text{C}$ ) and the certain

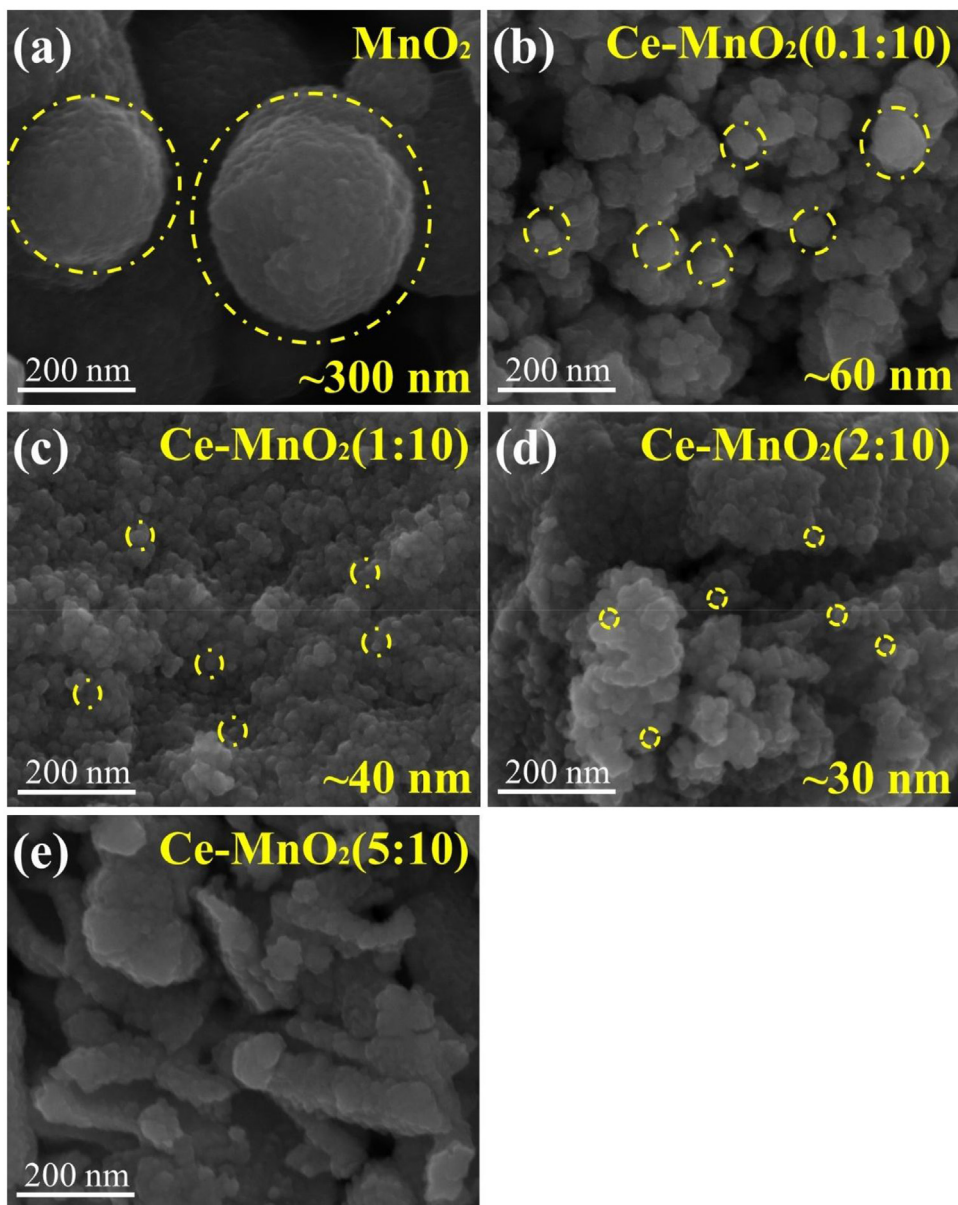


**Fig. 2.** FESEM images of as-prepared  $\text{MnO}_2$  and cerium-modified  $\text{MnO}_2$ : (a)  $\text{MnO}_2$ , (b)  $\text{Ce}-\text{MnO}_2(0.1:10)$ , (c)  $\text{Ce}-\text{MnO}_2(1:10)$ , (d)  $\text{Ce}-\text{MnO}_2(2:10)$ , (e)  $\text{Ce}-\text{MnO}_2(5:10)$ .

branch flow rate of synthesized air (25 mL/min). The total flow rate was 150 mL/min with the corresponding GHSV of  $\sim 90 \text{ L/g}_{\text{cat}} \cdot \text{h}$ . The concentration of HCHO was measured by using MBTH method. The outlet concentration of HCHO was calculated according to  $\text{CO}_2$  generation determined by a gas chromatograph (GC-2014, Shimadzu, Japan), which is a well-known method and precise enough to measure ppm level  $\text{CO}_2$ . The mineralization efficiency at high temperature was calculated as follows:

$$\text{Mineralization efficiency} (\%) = \frac{[\text{CO}_2]_{\text{out}}}{[\text{HCHO}]_{\text{in}}} \times 100\%$$

Where  $[\text{HCHO}]_{\text{in}}$  is the inlet HCHO concentration of the feed gas, and  $[\text{CO}_2]_{\text{out}}$  is the outlet  $\text{CO}_2$  concentration determined by gas chromatograph. Since no other carbon-containing compounds except  $\text{CO}_2$  in the products were detected by gas chromatograph, the mineralization efficiency can appropriately reflect the HCHO conversion at high temperature.

The activity of samples for low concentration HCHO at room temperature ( $25^\circ\text{C}$ ) was also measured. 100 mg samples (40–60

meshes) was exposed to an initial HCHO concentration of  $\sim 0.5 \text{ mg/m}^3$  ( $\sim 0.37 \text{ ppm}$ ) and total flow rate of 1 L/min with corresponding GHSV of  $600 \text{ L/g}_{\text{cat}} \cdot \text{h}$ . The relative humidity maintained at  $\sim 58\%$ . Both the inlet and outlet HCHO concentration were measured according to MBTH method, which is a standard method to measure low concentration HCHO. Since the inlet and outlet concentration of HCHO varied in a certain extent, it was measured for three times, and the average HCHO conversion with error bars was calculated accordingly. The HCHO conversion for low concentration at room temperature ( $25^\circ\text{C}$ ) was calculated as follows:

$$\text{HCHO conversion} (\%) = \frac{[\text{HCHO}]_{\text{in}} - [\text{HCHO}]_{\text{out}}}{[\text{HCHO}]_{\text{in}}} \times 100\%$$

Where  $[\text{HCHO}]_{\text{in}}$  is the inlet HCHO concentration of the feed gas, and  $[\text{HCHO}]_{\text{out}}$  is the outlet HCHO concentration measured by MBTH method.

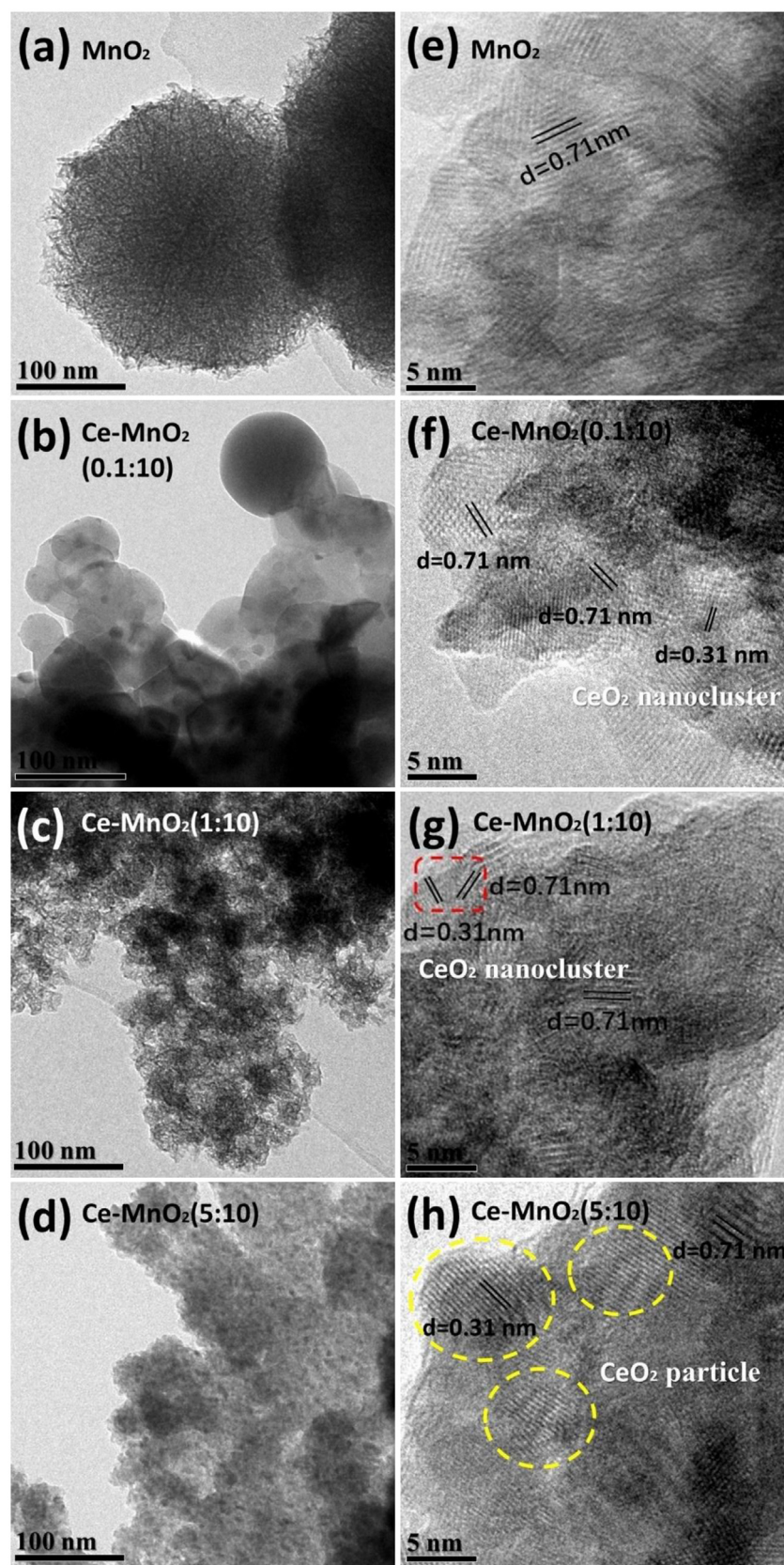


**Fig. 3.** TEM and HRTEM images of as-prepared  $\text{MnO}_2$  and cerium-modified  $\text{MnO}_2$  samples: (a,e)  $\text{MnO}_2$ , (b,f)  $\text{Ce}-\text{MnO}_2$  (0.1:10), (c,g)  $\text{Ce}-\text{MnO}_2$  (1:10), (d,h)  $\text{Ce}-\text{MnO}_2$  (5:10).

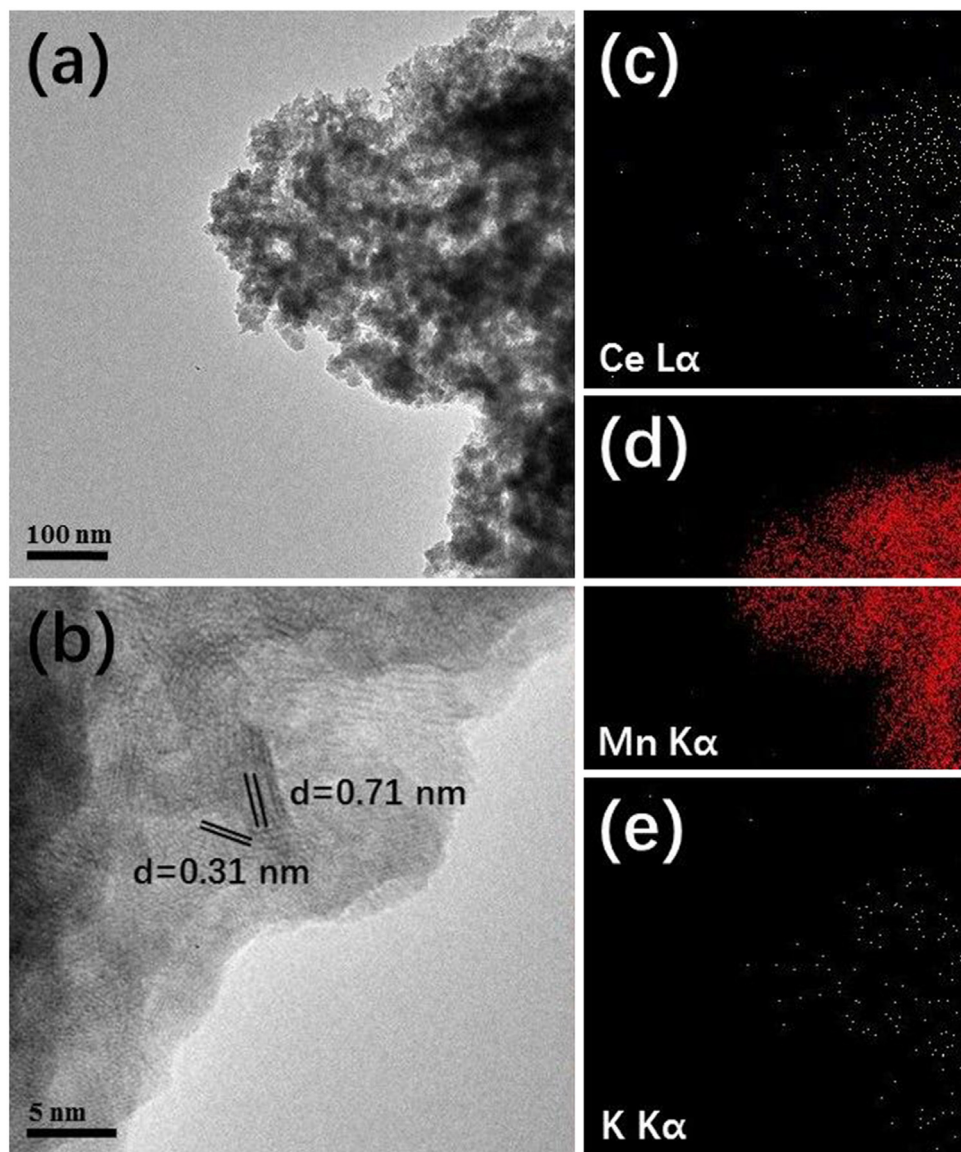


**Fig. 4.** TEM, HRTEM images and elemental mapping of as-prepared Ce-MnO<sub>2</sub>(1:10) sample.

**Table 1**

Combined results of BET specific surface area, chemical states of surface elements determined by XPS and elemental analysis determined by ICP-AES of as-synthesized samples.

Sample	Ce <sup>3+</sup> /Ce <sup>4+</sup>	Mn <sup>3+</sup> /Mn <sup>4+</sup>	O <sub>surf</sub> /O <sub>latt</sub>	Ce% (mass)	Mn% (mass)	K% (mass)	Ce/Mn (molar)	K/Mn (molar)	Surface area (m <sup>2</sup> /g)
MnO <sub>2</sub>	/	0.35	0.21	/	45.07	7.92	/	0.25	28.6
Ce-MnO <sub>2</sub> (0.1:10)	0.78	0.48	0.33	1.6	44.56	8.19	0.014	0.26	64.3
Ce-MnO <sub>2</sub> (1:10)	0.62	0.52	0.36	8.12	33.84	6.25	0.094	0.26	129.0
Ce-MnO <sub>2</sub> (2:10)	0.57	0.47	0.28	15.96	31.6	5.22	0.198	0.23	182.1
Ce-MnO <sub>2</sub> (5:10)	0.54	0.44	0.35	32.49	27.65	1.25	0.461	0.06	115.3

### 3. Results and discussion

#### 3.1. Morphology and phase structures

XRD patterns of as-synthesized samples were recorded to illustrate the phase structure (Fig. 1). The peaks of undoped material located around ~12.3°(001), ~24.6°(002), ~36.5°(100) and ~65.5°(110) were the characteristic peaks of the birnessite (*i.e.* δ-MnO<sub>2</sub>) structure (JCPDS No.80-1098) [29]. It can be seen from the XRD patterns the crystallinity was poor, thus the structure of man-

ganese oxide was ascribed to birnessite with a certain extent of amorphous state, which was confirmed by TEM observation shown in the following section. With the doping of cerium, the XRD patterns of materials remained hexagonal birnessite phase. However, the diffraction peaks ascribed to birnessite phase further became weaker as the cerium content further increased. Moreover, the diffraction peaks ascribed to cubic CeO<sub>2</sub> phase (JCPDS No.34-0394) could be clearly observed when the doping ratio reached 2:10. When the doping ratio increased to 5:10, only a broad and weak diffraction peak due to cubic CeO<sub>2</sub> phase was observed,

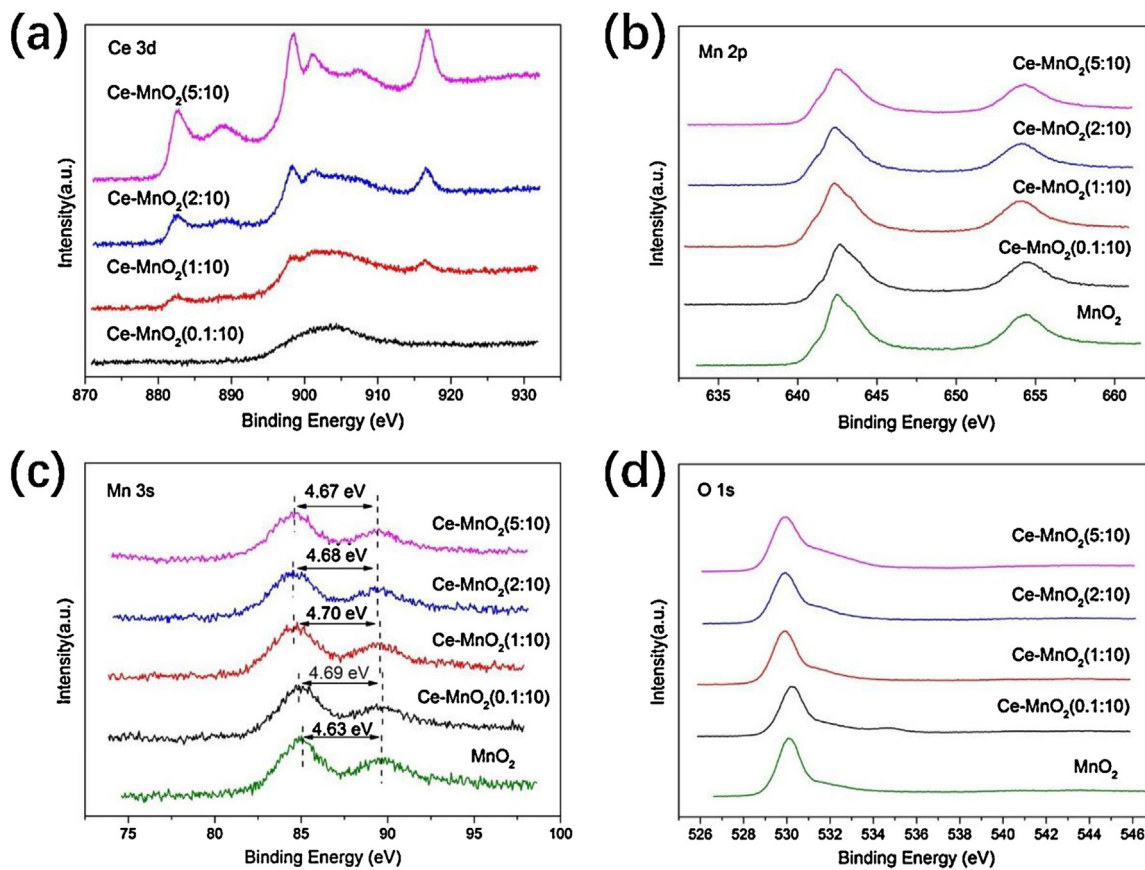


**Fig. 5.** XPS spectra of as-prepared  $\text{MnO}_2$  and cerium-modified  $\text{MnO}_2$  samples. (a) Ce 3d, (b) Mn 2p, (c) Mn 3s, (d) O 1s.

which implies that the crystal structure of birnessite was greatly destroyed as doping cerium increased. To further evaluate the effect of cerium modification, step-scan XRD analysis was carried out (Fig. S1). The  $2\theta$  angle of diffraction peak at  $12.2^\circ$  slightly decreases to  $12.0^\circ$  with doping of cerium, which means the interplane distance increases according to Bragg's law. This result can be ascribed to the replacement of  $\text{Mn}^{4+}$  ions in the lattice by larger ions such as  $\text{Mn}^{3+}$  or cerium ions.

The morphology of as-synthesized samples was surveyed by SEM, as shown in Fig. 2. Undoped birnessite samples were nanospheres composed of nanosheets. When the cerium content increased, the particle size of nanosphere consecutively decreased from  $\sim 300 \text{ nm}$  to  $\sim 30 \text{ nm}$ , which may lead to larger specific surface area. While the doping ratio further increased to 5:10, the spherical nanostructure collapsed and converted to irregular structure.

To further learn the structure change with cerium doping, TEM characterization was performed (Fig. 3). The lattice spacing of  $0.71 \text{ nm}$  observed on all samples was assigned to the (001) planes of birnessite. Besides, even when the doping ratio was as low as 0.1:10, the (111) planes of  $\text{CeO}_2$  with lattice spacing of  $0.31 \text{ nm}$  was also observed, which indicates that cerium ions also participated in the formation of the interface structure other than incorporation into the  $\text{MnO}_2$  bulk phase. The grain boundaries between  $\text{CeO}_2$  nanoclusters and  $\text{MnO}_2$  were observed in samples with the low doping ratio. While the doping ratio increased to 5:10,  $\text{CeO}_2$  particles became larger and presented separately from  $\text{MnO}_2$  particles.

Grain boundaries between different crystals on the surface of catalysts play a crucial role in catalytic reaction. There are coordinative unsaturated surface ions and vacancies among the grain boundaries, which contribute to the enhancement of oxygen mobility and activation of molecular oxygen [30–35]. Hojo et al. [32]

pointed out the role of oxygen vacancies in atomic structure of a  $\text{CeO}_2$  grain boundary. M. Sakai et al. [34] investigated the catalytic reduction of  $\text{NO}_x$  over  $\text{Cu}/\text{CeO}_2$  catalysts and mentioned that copper oxide species interacted with  $\text{CeO}_2$  in several forms: copper (II) ions, a greatly dispersed copper oxide film and large copper oxide particles. Among them, the greatly dispersed copper oxide film exhibited best catalytic activity.

There have been few reports about the interfacial structure of  $\text{MnO}_x\text{-CeO}_2$  composite and its interface active sites. In order to learn the dispersion of Ce, Mn and K in  $\text{Ce}\text{-MnO}_2(1:10)$  sample, the elemental mappings were conducted (Fig. 4). Besides the grain boundary between  $\text{CeO}_2$  nanocluster and  $\text{MnO}_2$  shown in Fig. 4(b), it can be seen that Ce and K were in a pretty high dispersion degree as well as Mn, confirming the incorporation of Ce into the bulk phase. The above results reveal that cerium species interacted with birnessite in two different forms: cerium ions incorporated into the  $\text{MnO}_2$  bulk phase, and  $\text{CeO}_2$  nanoclusters dispersed on the surface of  $\text{MnO}_2$ .

### 3.2. Physical and chemical properties of as-synthesized catalysts

The BET specific surface area of as-prepared samples is listed in Table 1. The undoped  $\text{MnO}_2$  possessed the smallest specific surface area ( $28.6 \text{ m}^2/\text{g}$ ). While it significantly increased to  $64.3\text{--}182.1 \text{ m}^2/\text{g}$  after cerium ions was doped. The drastic increase of specific surface area is ascribed to the size effect of as-prepared samples. As observed in SEM images, the particle size decreased from  $\sim 300 \text{ nm}$  of pure  $\text{MnO}_2$  to  $\sim 30 \text{ nm}$  of  $\text{Ce}\text{-MnO}_2(2:10)$ . The reduction of particle size due to addition of cerium ions implies that existence of cerium ions inhibits the growth of  $\text{MnO}_2$  crystal, which was also reported in literatures [36–38]. The reason can be

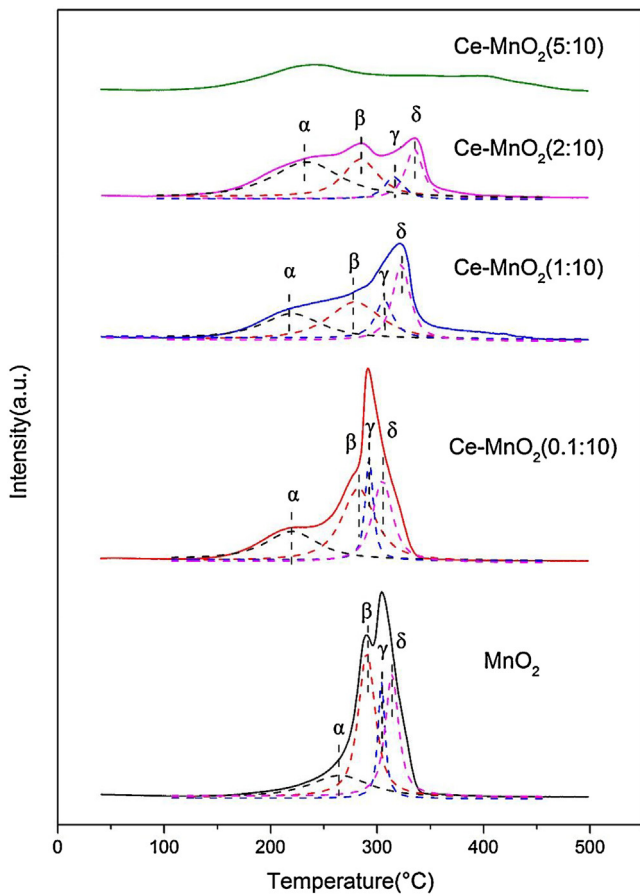
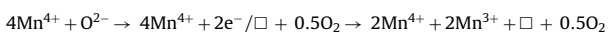


**Fig. 6.** H<sub>2</sub>-TPR profiles of as-prepared MnO<sub>2</sub> and cerium-modified MnO<sub>2</sub> samples.

explained as follows: after the replacement of manganese ions by cerium ions in the lattice the crystal structure deforms due to different radius of cerium from Mn<sup>4+</sup>, the continuing growth of crystal is affected. As a result, the crystal size becomes smaller. When the doping ratio of Ce/Mn further increased to 5:10, the birnessite structure collapsed as reflected by the great reduction of the K/Mn molar ratio (**Table 1**) and its specific surface area accordingly decreased to 115.3 m<sup>2</sup>/g.

XPS patterns of as-synthesized samples are shown in **Fig. 5**. Surface chemical compositions and chemical states are summarized in **Table 1**. **Fig. 5(a)** indicates that the intensity of peaks assigned to Ce 3d increased with doping of cerium. Furthermore, the molar ratio of Ce<sup>3+</sup> to Ce<sup>4+</sup> decreased with increasing doping ratio of cerium.

The Mn 2p XPS spectra for cerium-birnessite samples is shown in **Fig. 5(b)**. It exhibited two peaks at ~642.4 eV and ~654.0 eV, which are respectively assigned to Mn2p<sub>3/2</sub> and Mn2p<sub>1/2</sub>. After the curve-fitting analysis of Mn2p<sub>3/2</sub>, the ratio of Mn<sup>3+</sup>/Mn<sup>4+</sup> was calculated by their peak areas [39,40], and the results were summarized in **Table 1**. As discussed in the literature [41], oxygen vacancies would be generated to maintain electrostatic balance once Mn<sup>3+</sup> appeared in the catalyst as following:



where  $\square$  represents an oxygen vacancy in the lattice. Thus, the higher ratio of Mn<sup>3+</sup>/Mn<sup>4+</sup> means the higher content of oxygen vacancies, which play important roles as active sites for oxidation reactions. Among all samples, the Ce-MnO<sub>2</sub>(1:10) sample owned the highest Mn<sup>3+</sup>/Mn<sup>4+</sup> ratio (0.52), implying Ce-MnO<sub>2</sub> (1:10) had largest amount of oxygen vacancies to maintain electrostatic balance due to Mn<sup>3+</sup> [42,43]. The Mn 3s XPS spectra for as-synthesized samples are shown in **Fig. 5(c)**. According to an empirical equation,

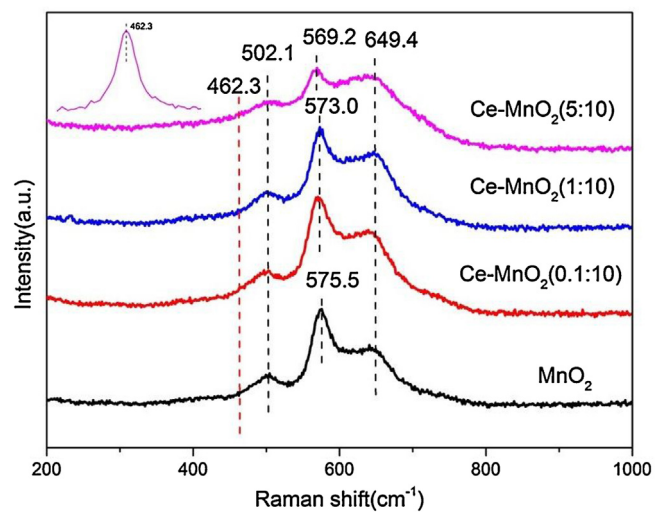


**Fig. 7.** Raman spectra of as-prepared MnO<sub>2</sub> and cerium-modified MnO<sub>2</sub> samples. The inset is enlarged characteristic peak of Ce—O vibration of Ce-MnO<sub>2</sub>(5:10).

i.e. average oxidation state, AOS = 8.956 – 1.126 × ΔE [38,44–46], the average oxidation state could be calculated by the energy differences (ΔE) between two peaks in the corresponding Mn 3s XPS spectra. The ratios of Mn<sup>3+</sup>/Mn<sup>4+</sup> calculated from Mn 3s results were consistent with those from Mn 2p.

The O 1s XPS spectra for as-synthesized samples shown in **Fig. 5(d)** can be deconvoluted into three peaks at 529.9–530.2 eV, 530.7–531.5 eV and 533.0–533.7 eV, corresponding to lattice oxygen (O<sub>latt</sub>), surface adsorbed oxygen species (such as O<sub>2</sub><sup>−</sup>, O<sup>−</sup> and OH group) and adsorbed molecular H<sub>2</sub>O [40]. The curve-fitting analysis of O 1s XPS spectra revealed that lattice oxygen and surface adsorbed oxygen were the predominant species on the surface of samples. The Ce-MnO<sub>2</sub>(1:10) sample owned the largest O<sub>surf</sub>/O<sub>latt</sub> ratio (0.36) among doped materials while the Ce-MnO<sub>2</sub>(2:10) sample exhibited the least (0.28). It has been pointed out in literatures [3,4,7,47,48], surface adsorbed oxygen played a key role in HCHO oxidation. Surface adsorbed oxygen species tends to participate into the oxidation reaction due to its high activity and the interaction between catalyst surface and reactant [49,50], while lattice oxygen species with high mobility enhanced the formation of surface active oxygen species through the complex migration between surface lattice oxygen and oxygen vacancy with molecular oxygen [51]. The reaction pathway of HCHO oxidation will also be discussed in the following *in situ* DRIFTS results.

The elemental analysis by ICP-AES revealed that real doping ratio was consistent with the nominal doping ratio. The ratio of K to Mn (K/Mn) was compared to learn the transformation of birnessite structure after doping of cerium. The K/Mn ratio little changed (~0.26) among samples at a low doping ratio, which indicates that the birnessite structure maintained with low content of cerium incorporation into its lattice. While the doping ratio increased to 5:10, the K/Mn ratio decreased to 0.06, which can be ascribed to the collapse of birnessite structure. With large loss of potassium ions, the hexagonal birnessite structure was destroyed as reflected by XRD analysis.

The reducibility of as-prepared samples was evaluated by H<sub>2</sub>-TPR to distinguish the catalytic activity of surface adsorbed oxygen. As shown in **Fig. 6**, the TPR profiles of as-synthesized samples are divided into four peaks, marked as α, β, γ and δ. α peak represents the consumption of surface adsorbed oxygen species. In addition, β, γ and δ peaks with the peak area ratio of 3:1:2 could be assigned to successive reductions of K<sub>x</sub>MnO<sub>2</sub> → Mn<sub>2</sub>O<sub>3</sub> → Mn<sub>3</sub>O<sub>4</sub> → MnO, respectively [52,53]. With the increasing content of cerium in samples, the consumption of hydrogen showed a trend of rise first then

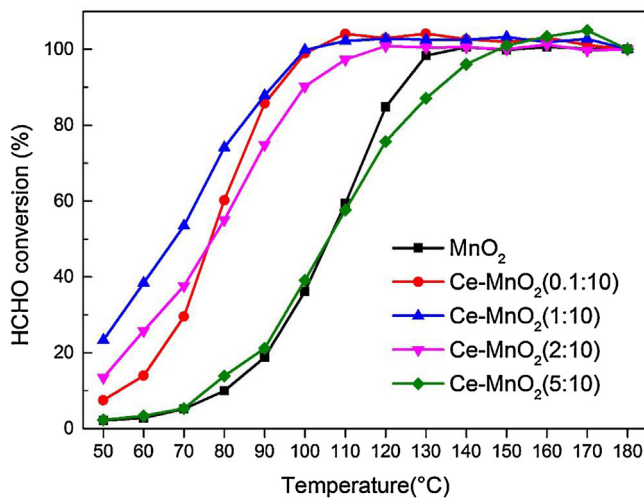


**Fig. 8.** Temperature dependence of HCHO conversions over as-synthesized catalysts: HCHO = 190 ppm, O<sub>2</sub> = 20%, N<sub>2</sub> balance, GHSV = 90 L/g<sub>cat</sub>·h.

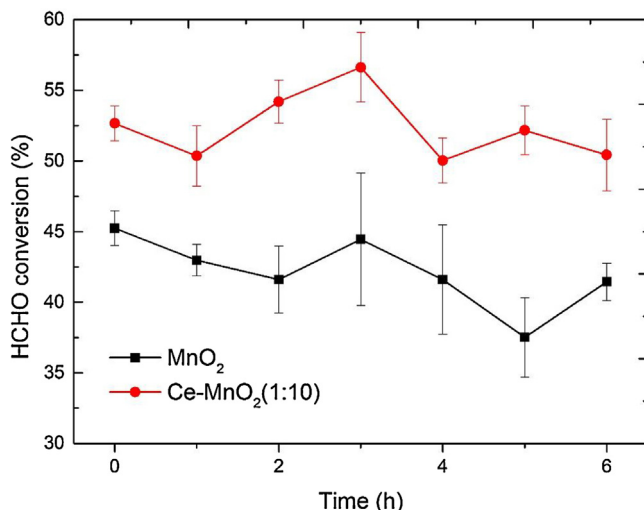


**Fig. 9.** The removal efficiency of HCHO over MnO<sub>2</sub> and Ce-MnO<sub>2</sub>(1:10) at room temperature (25 °C): HCHO = ~0.5 mg/m<sup>3</sup> (~0.37 ppm), O<sub>2</sub> = 20%, N<sub>2</sub> balance, RH = ~58%, GHSV = 600 L/g<sub>cat</sub>·h.

fall among MnO<sub>2</sub> (7.63 mmol/g), Ce-MnO<sub>2</sub>(0.1:10) (7.85 mmol/g), Ce-MnO<sub>2</sub>(1:10) (6.71 mmol/g), Ce-MnO<sub>2</sub>(2:10) (6.67 mmol/g) and Ce-MnO<sub>2</sub>(5:10) (6.56 mmol/g). The peak of Ce-MnO<sub>2</sub>(5:10) was totally different from the peak of birnessite and Ce-MnO<sub>2</sub> at low doping ratio due to its collapse structure and different chemical property. After doping of cerium, both  $\alpha$  and  $\beta$  peaks moved to lower temperatures and  $\alpha$  peak had larger area, which indicates that doping cerium improves the reducibility of surface adsorbed oxygen species and mobility of lattice oxygen [54,55].

Fig. 7 shows the Raman spectra of as-synthesized samples. The major peaks could be found at 500–510, 575–585 and 625–650 cm<sup>-1</sup>, which are attributed to the (Mn–O–Mn) flexural vibration of MnO<sub>6</sub> groups, the stretching vibration  $\nu_3$ (Mn–O) in the basal plane of [MnO<sub>6</sub>] sheets and the symmetric stretching vibration  $\nu_2$ (Mn–O) of MnO<sub>6</sub> groups, respectively [56]. The peak intensity ratio between peak at 575–585 cm<sup>-1</sup> and peak at 649.4 cm<sup>-1</sup> decreased as the content of cerium increased, as well as the redshift of peak at 575–585 cm<sup>-1</sup>. These results can be ascribed to the effect of cerium species incorporation into the bulk phase. The larger radius of cerium ion and increasing defects led to the stress in birnessite, manifesting the broader peak in Raman spectra

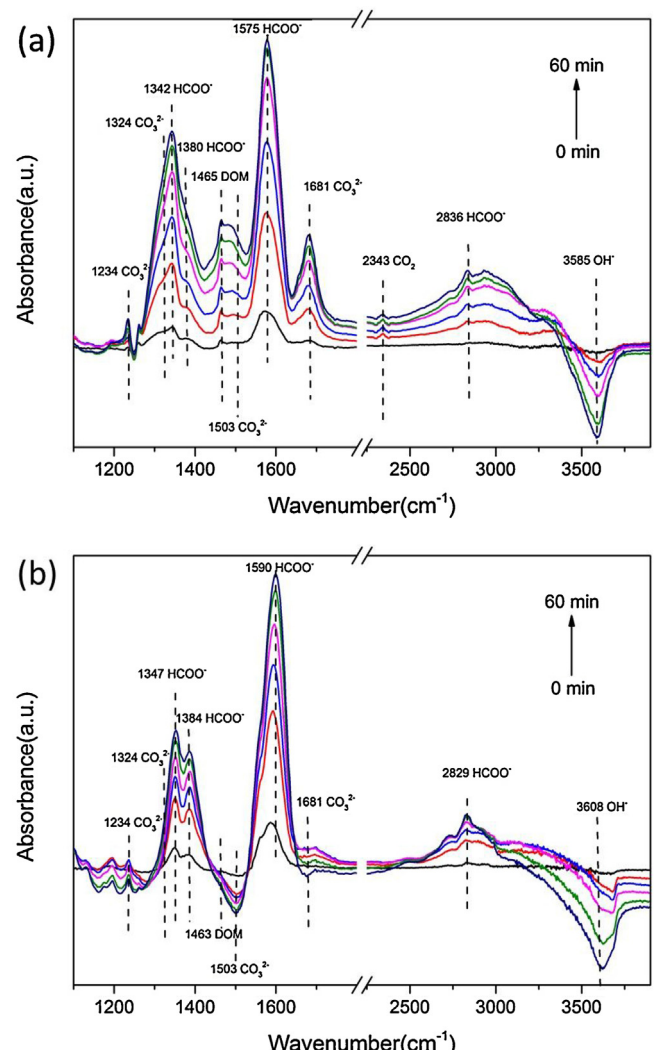


**Fig. 10.** *In situ* DRIFTS spectra of (a) MnO<sub>2</sub> and (b) Ce-MnO<sub>2</sub>(1:10) exposed to the flow of 80 ppm HCHO/synthesized air for 60 min at room temperature (25 °C).

and the redshift of weaker peak assigned to  $\nu_3$ (Mn–O). The Raman spectra about Ce–O was also investigated (Fig. S2). The characteristic peak of Ce–O located at ~462 cm<sup>-1</sup>. The characteristic peak was only observed in the sample of Ce-MnO<sub>2</sub>(5:10). The absence of this peak in other samples with lower content of cerium could be explained by that the majority of cerium incorporated into the bulk phase. Too low amount of cerium on the surface of sample may cause no characteristic peak in Raman spectra. This result also confirms that cerium species interacted with birnessite in two different ways mentioned above.

### 3.3. HCHO removal activity

Fig. 8 shows the performance of as-prepared samples for HCHO oxidation at different temperatures. The HCHO removal activity was evaluated with an initial HCHO concentration of 190 ppm and total flow rate of 150 mL/min with corresponding GHSV of 90 L/g<sub>cat</sub>·h. The complete conversion of HCHO over undoped birnessite sample was achieved at 130 °C. The catalytic activity of doped samples was improved. The catalytic oxidation over Ce-MnO<sub>2</sub>(0.1:10) and Ce-MnO<sub>2</sub>(1:10) both exhibited 100% conversion at 100 °C, while the latter exhibited higher activity at lower temperature, which is meaningful for HCHO removal in indoor environment. The complete conversion temperature over

**Table 2**Summarization of literature data on HCHO catalytic oxidation over  $\text{MnO}_x\text{-CeO}_2$  composite catalysts at low temperature.

Catalyst	Ce/Mn	Preparation conditions	Test conditions	$T_{50\%}$	$T_{100\%}$	Ref.
Ce-MnO <sub>2</sub> (1:10)	0.1	shaken in a water bath (90 °C) at a frequency of 150 rpm for 10 h; dried at 105 °C for 12 h	190 ppm HCHO, 20% O <sub>2</sub> , N <sub>2</sub> balance, GHSV ~ 90 L/g <sub>cat</sub> ·h	~70	100	This work
			580 ppm HCHO, 20% O <sub>2</sub> , N <sub>2</sub> balance, GHSV ~ 30 L/g <sub>cat</sub> ·h	~70	100	
MnO <sub>x</sub> -CeO <sub>2</sub> (MP-773)	1	stirred at 50 °C for 2 h; dried at 110 °C for 12 h; calcined at 500 °C for 6 h	580 ppm HCHO, 18% O <sub>2</sub> , He balance, GHSV ~ 30 L/g <sub>cat</sub> ·h	>80	100	[23]
Ag/MnO <sub>x</sub> -CeO <sub>2</sub>	1	stirred at 50 °C for 2 h; dried at 110 °C for 12 h; calcined at 500 °C for 6 h	580 ppm HCHO, 18% O <sub>2</sub> , He balance, GHSV ~ 30 L/g <sub>cat</sub> ·h	~70	100	[24]
Pt/MnO <sub>x</sub> -CeO <sub>2</sub>	1	stirred at 50 °C for 2 h; dried at 110 °C for 12 h; calcined at 500 °C for 6 h	30 ppm HCHO, 20% O <sub>2</sub> , He balance, GHSV ~ 30 L/g <sub>cat</sub> ·h	/	RT	[25]
MnO <sub>x</sub> -CeO <sub>2</sub> (CeMn80)	0.25	stirred at 50 °C for 2 h; dried at 110 °C overnight; calcined at 400 °C for 6 h	580 ppm HCHO, 20% O <sub>2</sub> , N <sub>2</sub> balance, GHSV ~ 30 L/g <sub>cat</sub> ·h	>75	100	[27]
MnO <sub>x</sub> -CeO <sub>2</sub> -acid treated	0 ~ 1	stirred at 75 °C for 1 h; heated at 75 °C for 12 h; calcined at 500 °C for 6 h; treated with acid for 1 h and dried at 105 °C	400 ppm HCHO, 20% O <sub>2</sub> , He balance, GHSV ~ 30 L/g <sub>cat</sub> ·h	/	>100	[26]

Ce-MnO<sub>2</sub>(2:10) was 110 °C. Owing to the collapsed structure of Ce-MnO<sub>2</sub>(5:10), the temperature required for complete oxidation of HCHO was 140 °C, which had similar activity to that of undoped birnessite sample at lower temperature.

According to the HCHO oxidation conversion mentioned above, doping of cerium obviously promoted the catalytic activity towards HCHO oxidation. The promoting effect of cerium doping can be ascribed to more oxygen vacancies generated, which act as active sites for HCHO oxidation. As observed in SEM images, with the doping of cerium ions, the particle size of catalysts became smaller, which leads to higher specific surface area as confirmed by BET measurement. The higher specific surface area facilitates the exposure of active sites. Moreover, smaller particle makes more Mn atoms exposed and coordinative unsaturated Mn atoms may accordingly increase. In the meanwhile, at low doping ratio of cerium, the grain boundaries formed between MnO<sub>2</sub> and CeO<sub>2</sub> nanoclusters as observed by TEM, which further increases the exposure of active sites for reaction. Taking all points mentioned above into account, Ce-MnO<sub>2</sub>(1:10) catalyst showed the highest ratio of Mn<sup>3+</sup>/Mn<sup>4+</sup>, i.e. this catalyst might possess the highest amount of oxygen vacancies as active sites, which is evidenced by its highest O<sub>surf</sub>/O<sub>latt</sub> ratio as revealed by XPS analysis. As a result, Ce-MnO<sub>2</sub>(1:10) catalyst owned the best HCHO removal activity among as-synthesized catalysts. The above result suggests that the oxygen vacancies of MnO<sub>2</sub> played a key role in catalytically active sites instead of oxygen vacancies of CeO<sub>2</sub>. Doping cerium tends to improve the activity indirectly by adjusting the amount of Mn<sup>3+</sup> species, and it seems that the amount of Mn<sup>3+</sup> species is an indicator of the active sites on the surface.

As reported in the literatures shown in Table 2, the material of Tang et al. [23] showed the best activity among the previous research towards catalytic oxidation of HCHO over MnO<sub>x</sub>-CeO<sub>2</sub> composite catalysts, which exhibited ~50% HCHO conversion at 80 °C and achieved complete HCHO conversion at 100 °C. The catalyst synthesized by Tang et al. was treated at 500 °C with a ratio between cerium and manganese of ~1:1, and tested with higher inlet HCHO concentration (~580 ppm) and lower gas hourly space velocity (GHSV) (~30 L/g<sub>cat</sub>·h). To compare with the catalyst synthesized by Tang et al. mentioned above, the Ce-MnO<sub>2</sub>(1:10) catalyst was also evaluated under the same reaction conditions. The Ce-MnO<sub>2</sub>(1:10) catalyst synthesized in this work showed better HCHO removal activity ( $T_{50\%} = 70$  °C) at low temperature than

the other ( $T_{50\%} = 80$  °C). Thus, compared with the results summarized in Table 2, the Ce-MnO<sub>2</sub>(1:10) catalyst, without doping of noble metal, exhibited better HCHO oxidation activity than other MnO<sub>x</sub>-CeO<sub>2</sub> composite catalysts due to more active sites on the surface.

Taking practical condition of air cleaning system into account, HCHO of ~0.5 mg/m<sup>3</sup> (~0.37 ppm) and GHSV of 600 L/g<sub>cat</sub>·h were set to confirm the removal efficiency of as-prepared catalysts at room temperature. Fig. 9 illustrated the HCHO removal efficiency over undoped birnessite catalyst and the Ce-MnO<sub>2</sub>(1:10). Both samples kept stable during 6 h test. The Ce-MnO<sub>2</sub>(1:10) catalyst exhibited the removal ratio of ~52%, which was much higher than the undoped birnessite sample (~43%). These results indicate that the Ce-MnO<sub>2</sub>(1:10) catalyst not only has high activity at high temperature but also owns significant activity for HCHO oxidation at ambient temperature. Thus, Ce-MnO<sub>2</sub>(1:10) has practical value in indoor air purification.

The high activity of Ce-MnO<sub>2</sub>(1:10) for HCHO oxidation at ambient temperature is also confirmed by *in situ* DRIFTS. As-synthesized samples were exposed to the flow of HCHO with inlet concentration of 80 ppm and flow rate of 30 mL/min, which was balanced with synthesized air. The intermediate species on the surface of catalyst within 60 min were observed as shown in Fig. 10. Peaks located around 1342–1347, 1380–1384, 1575–1590 and 2829–2836 cm<sup>-1</sup> can be assigned to  $\nu_s(\text{COO}^-)$ ,  $\delta(\text{CH})$ ,  $\nu_{as}(\text{COO}^-)$  and  $\nu(\text{CH})$  of formate species [26,57,58]. The peaks located at 1234, 1324, 1503 and 1681 cm<sup>-1</sup> are assigned to  $\nu_{as}(\text{COO})$ ,  $\nu_s(\text{COO}^-)$ ,  $\nu_{as}(\text{COO}^-)$  and  $\nu(\text{C=O})$  of carbonate species [59]. And the peaks located around 1463–1465, 2343, 3585–3608 cm<sup>-1</sup> are assigned to dioxymethylene (DOM) species, adsorbed carbon dioxide and hydroxyl groups, respectively [3,60]. In comparison with undoped birnessite sample, no DOM species were accumulated on the surface of Ce-MnO<sub>2</sub>(1:10) and less carbonate species formed. As reported in literatures, when HCHO is catalytically oxidized by noble metals or metal oxides, generally HCHO is first transformed into DOM, and then further into formate, carbonate and carbon dioxide. No accumulation of DOM implies HCHO was oxidized much faster over Ce-MnO<sub>2</sub>(1:10) surface than on the surface of undoped birnessite. Similarly, less accumulation of carbonate species over Ce-MnO<sub>2</sub>(1:10) means these species transform or desorb faster over Ce-MnO<sub>2</sub>(1:10) surface. On both Ce-MnO<sub>2</sub>(1:10) and undoped birnessite sample, with the oxidation of HCHO, the peaks

corresponding to surface hydroxyl groups gradually negatively increased, which means HCHO oxidation is closely related with the consumption of surface hydroxyl groups. These phenomena have also been observed in our previous research [20]. Nevertheless, Ce-MnO<sub>2</sub>(1:10) exhibited better activity and less intermediates were accumulated on its surface due to its higher content of oxygen vacancies.

#### 4. Conclusions

Cerium modified birnessite-type MnO<sub>2</sub> samples (Ce-MnO<sub>2</sub>) with different doping ratios were obtained via a redox reaction between potassium permanganate and ammonia oxalate at 90 °C with addition of cerium nitrate. At a low doping ratio (~1–10%), the growth and assembly of birnessite crystal is inhibited and its crystallinity become poorer, resulting in smaller nanoparticles with larger specific surface area. In addition, cerium dioxide (CeO<sub>2</sub>) nanocluster was simultaneously formed, resulting in close contact and grain boundary with MnO<sub>2</sub>. Cerium-doped birnessite owned higher ratio of surface adsorbed oxygen species, the reducibility and mobility of surface and lattice oxygen were improved. The determining factor leading to high catalytic activity was ascribed to more active sites on the surface due to doping cerium. As-synthesized Ce-MnO<sub>2</sub>(1:10) catalyst showed the best activity for HCHO removal, obtaining the complete mineralization of 190 ppm HCHO at 100 °C and the GHSV of 90 L/g<sub>cat</sub>·h. Furthermore, Ce-MnO<sub>2</sub>(1:10) also showed much higher activity for low concentration HCHO (~0.5 mg/m<sup>3</sup>, i.e. ~0.37 ppm) at room temperature than undoped birnessite sample, indicating that cerium-doped birnessite is of practical value in indoor air purification.

#### Acknowledgment

This work was financially supported by Natural Science Foundation (21677083, 21521064) and Tsinghua University Initiative Scientific Research Program (20131089251).

#### Appendix A. Supplementary data

Supplementary data associated with this article can be found, in the online version, at <http://dx.doi.org/10.1016/j.apcatb.2017.04.025>.

#### References

- [1] T. Saltherammer, S. Mentese, R. Marutzky, Chem. Rev. 110 (2010) 2536–2572.
- [2] J. Quiroz Torres, S. Royer, J.P. Bellat, J.M. Giraudon, J.F. Lamonier, ChemSusChem 6 (2013) 578–592.
- [3] C. Zhang, F. Liu, Y. Zhai, H. Ariga, N. Yi, Y. Liu, K. Asakura, M. Flytzani-Stephanopoulos, H. He, Angew. Chem. Int. Ed. 51 (2012) 9628–9632.
- [4] L. Nie, J. Yu, X. Li, B. Cheng, G. Liu, M. Jaroniec, Environ. Sci. Technol. 47 (2013) 2777–2783.
- [5] H. Huang, D.Y.C. Leung, ACS Catal. 1 (2011) 348–354.
- [6] C. Zhang, Y. Li, Y. Wang, H. He, Environ. Sci. Technol. 48 (2014) 5816–5822.
- [7] B.-b. Chen, X.-b. Zhu, M. Crocker, Y. Wang, C. Shi, Appl. Catal. B: Environ. 154 (2014) 73–81.
- [8] Q. Xu, W. Lei, X. Li, X. Qi, J. Yu, G. Liu, J. Wang, P. Zhang, Environ. Sci. Technol. 48 (2014) 9702–9708.
- [9] S.J. Park, I. Bae, I.-S. Nam, B.K. Cho, S.M. Jung, J.-H. Lee, Chem. Eng. J. 195 (2012) 392–402.
- [10] J. Pei, J.S. Zhang, HVACR Res. 17 (2011) 476–503.
- [11] H. Huang, Y. Xu, Q. Feng, D.Y. Leung, Catal. Sci. Technol. 5 (2015) 2649–2669.
- [12] Y. Sekine, Atmos. Environ. 36 (2002) 5543–5547.
- [13] H. Chen, J. He, C. Zhang, H. He, J. Phys. Chem. C 111 (2007) 18033–18038.
- [14] H. Tian, J. He, X. Zhang, L. Zhou, D. Wang, Microporous Mesoporous Mat. 138 (2011) 118–122.
- [15] C. Shi, Y. Wang, A. Zhu, B. Chen, C. Au, Catal. Commun. 28 (2012) 18–22.
- [16] J. Miyawaki, G.-H. Lee, J. Yeh, N. Shiratori, T. Shimohara, I. Mochida, S.-H. Yoon, Catal. Today 185 (2012) 278–283.
- [17] R. Averlant, S. Royer, J.M. Giraudon, J.P. Bellat, I. Bezverkhyy, G. Weber, J.F. Lamonier, ChemCatChem 6 (2014) 152–161.
- [18] J. Zhang, Y. Li, L. Wang, C. Zhang, H. He, Catal. Sci. Technol. 5 (2015) 2305–2313.
- [19] T. Chen, H. Dou, X. Li, X. Tang, J. Li, J. Hao, Microporous Mesoporous Mat. 122 (2009) 270–274.
- [20] J. Wang, P. Zhang, J. Li, C. Jiang, R. Yunus, J. Kim, Environ. Sci. Technol. 49 (2015) 12372–12379.
- [21] J. Wang, D. Li, P. Li, P. Zhang, Q. Xu, J. Yu, RSC Adv. 5 (2015) 100434–100442.
- [22] Y. Lou, X.-M. Cao, J. Lan, L. Wang, Q. Dai, Y. Guo, J. Ma, Z. Zhao, Y. Guo, P. Hu, Chem. Commun. 50 (2014) 6835–6838.
- [23] X. Tang, Y. Li, X. Huang, Y. Xu, H. Zhu, J. Wang, W. Shen, Appl. Catal. B: Environ. 62 (2006) 265–273.
- [24] X. Tang, J. Chen, Y. Li, Y. Li, Y. Xu, W. Shen, Chem. Eng. J. 118 (2006) 119–125.
- [25] X. Tang, J. Chen, X. Huang, Y. Xu, W. Shen, Appl. Catal. B: Environ. 81 (2008) 115–121.
- [26] J. Quiroz, J.-M. Giraudon, A. Gervasini, C. Dujardin, C. Lancelot, M. Trentesaux, J.-F. Lamonier, ACS Catal. 5 (2015) 2260–2269.
- [27] L. Xuesong, L. Jiqing, Q. Kun, W. Huang, L. Mengfei, J. Rare Earths 27 (2009) 418–424.
- [28] E.A. Johnson, J.E. Post, Am. Mineral. 91 (2006) 609–618.
- [29] J.E. Post, D.R. Vebben, Am. Mineral. 75 (1990) 477–489.
- [30] S. Royer, D. Duprez, S. Kaliaguine, J. Catal. 234 (2005) 364–375.
- [31] R. Vidruk, M.V. Landau, M. Herskowitz, M. Talianker, N. Frage, V. Ezersky, N. Froumin, J. Catal. 263 (2009) 196–204.
- [32] H. Hojo, T. Mizoguchi, H. Ohta, S.D. Findlay, N. Shibata, T. Yamamoto, Y. Ikutara, Nano Lett. 10 (2010) 4668–4672.
- [33] Q. Fu, W.-X. Li, Y. Yao, H. Liu, H.-Y. Su, D. Ma, X.-K. Gu, L. Chen, Z. Wang, H. Zhang, Science 328 (2010) 1141–1144.
- [34] M. Sakai, Y. Nagai, Y. Aoki, N. Takahashi, Appl. Catal. A: Gen. 510 (2016) 57–63.
- [35] W. Gac, G. Słowiak, W. Zawadzki, Appl. Surf. Sci. 370 (2016) 536–544.
- [36] L. Sun, Q. Cao, B. Hu, J. Li, J. Hao, G. Jing, X. Tang, Appl. Catal. A: Gen. 393 (2011) 323–330.
- [37] X. Xiao, S.P. Sun, M. McBride, A. Lemley, Environ. Sci. Pollut. R. 20 (2013) 10–21.
- [38] L. Zhang, J. Tu, L. Lyu, C. Hu, Appl. Catal. B: Environ. 181 (2016) 561–569.
- [39] M.C. Biesinger, B.P. Payne, A.P. Grosvenor, L.W. Lau, A.R. Gerson, R.S.C. Smart, Appl. Surf. Sci. 257 (2011) 2717–2730.
- [40] T. Mathew, K. Suzuki, Y. Ikuta, N. Takahashi, H. Shinjoh, Chem. Commun. 48 (2012) 10987–10989.
- [41] X. Liu, K. Zhou, L. Wang, B. Wang, Y. Li, J. Am. Chem. Soc. 131 (2009) 3140–3141.
- [42] H. Wang, J. Zhang, X. Hang, X. Zhang, J. Xie, B. Pan, Y. Xie, Angew. Chem. 127 (2015) 1211–1215.
- [43] J. Hou, Y. Li, M. Mao, L. Ren, X. Zhao, ACS Appl. Mater. Interfaces. 6 (2014) 14981–14987.
- [44] V. Galakhov, M. Demeter, S. Bartkowski, M. Neumann, N. Ovechkina, E. Kurmaev, N. Lobachevskaya, Y.M. Mukovskii, J. Mitchell, D. Ederer, Phys. Rev. B 65 (2002) 113102.
- [45] V. Santos, M. Pereira, J. Orfao, J. Figueiredo, Appl. Catal. B: Environ. 88 (2009) 550–556.
- [46] J. Wang, R. Yunus, J. Li, P. Li, J. Kim, Appl. Surf. Sci. 357 (2015) 787–794.
- [47] H. Over, A. Seitsonen, Science 297 (2002) 2003–2005.
- [48] B. Bai, J. Li, ACS Catal. 4 (2014) 2753–2762.
- [49] M. Setvíñ, U. Aschauer, P. Scheiber, Y.F. Li, W. Hou, M. Schmid, A. Selloni, U. Diebold, Science 341 (2013) 988–991.
- [50] G.I. Panov, K.A. Dubkov, E.V. Starokon, Catal. Today 117 (2006) 148–155.
- [51] J. Wang, J. Li, C. Jiang, P. Zhou, P. Zhang, J. Yu, Appl. Catal. B: Environ. 204 (2017) 147–155.
- [52] Y. Yang, J. Huang, S. Zhang, S. Wang, S. Deng, B. Wang, G. Yu, Appl. Catal. B: Environ. 150 (2014) 167–178.
- [53] P. Hu, Z. Amghouz, Z. Huang, F. Xu, Y. Chen, X. Tang, Environ. Sci. Technol. 49 (2015) 2384–2390.
- [54] Y. Wang, H. Liu, P. Hu, Z. Huang, J. Gao, F. Xu, Z. Ma, X. Tang, Catal. Lett. 145 (2015) 1880–1884.
- [55] Y. Chen, Z. Huang, P. Hu, J. Chen, X. Tang, Catal. Commun. 75 (2016) 74–77.
- [56] C. Julien, M. Massot, R. Baddour-Hadjean, S. Franger, S. Bach, J. Pereira-Ramos, Solid State Ionics 159 (2003) 345–356.
- [57] Z. Yan, Z. Xu, J. Yu, M. Jaroniec, Environ. Sci. Technol. 49 (2015) 6637–6644.
- [58] C. Shi, B.-b. Chen, X.-s. Li, M. Crocker, Y. Wang, A.m. Zhu, Chem. Eng. J. 200 (2012) 729–737.
- [59] A.A. Davydov, C.H. Rochester, Infrared Spectroscopy of Adsorbed Species on the Surface of Transition Metal Oxides, Wiley, 1990.
- [60] H.D. Lutz, Bonding and Structure of Water Molecules in Solid Hydrates. Correlation of Spectroscopic and Structural Data, Solid Materials, Springer, 1988, pp. 97–125.